

- Czochralski and web crystals," in *Proc. 12th Photovoltaic Specialists Conf.*, pp. 106-111, 1976.
- [15] E. Kuroda and T. Saitoh, "Growth and characterization of polycrystalline silicon ingots from metallurgical-grade source material," *J. Crystal Growth.*, vol. 47, no. 2, pp. 251-260, 1979.
- [16] H. J. Hovel, *Semiconductors and Semimetals*, vol. 11, *Solar Cells*. New York: Academic Press, 1975.
- [17] L. M. Terman, "Spectral response of solar-cell structures," *Solid-State Electron.*, vol. 2, pp. 1-7, 1961.
- [18] H. Kressel, "A review of the effect of imperfections on the electrical breakdown of p-n junctions," *RCA Rev.*, pp. 175-206, June, 1967.
- [19] S. M. Hu, "Dislocation pinning effect of oxygen atoms in silicon," *Appl. Phys. Lett.*, vol. 31, no. 2, pp. 53-55, 1977.

## Impurities in Silicon Solar Cells

JOHN RANSFORD DAVIS, JR., MEMBER, IEEE, AJEET ROHATGI, MEMBER, IEEE, RICHARD H. HOPKINS, PHILLIP D. BLAIS, MEMBER, IEEE, P. RAI-CHOUDHURY, SENIOR MEMBER, IEEE, JAMES R. MCCORMICK, MEMBER, IEEE, AND H. C. MOLLENKOPF

**Abstract**—The effects of various metallic impurities, both singly and in combinations, on the performance of silicon solar cells have been studied. Czochralski crystals were grown with controlled additions of secondary impurities. The primary dopants were boron and phosphorus while the secondaries were: Al, B, C, Ca, Co, Cr, Cu, Fe, Mg, Mn, Mo, Nb, P, Pd, Ta, Ti, V, W, Zn, and Zr. Impurity concentrations ranged from  $10^{10}$  to  $10^{17}/\text{cm}^3$ . Solar cells were made using a conventional diffusion process and were characterized by computer reduction of  $I$ - $V$  data. The collected data indicated that impurity-induced performance loss was primarily due to reduction of the base diffusion length. Based on this observation, an analytic model was developed which predicts cell performance as a function of the secondary impurity concentrations. The calculated performance parameters are in good agreement with measured values except for Cu, Ni, and Fe, which at higher concentrations, degrade the cell substantially by means of junction mechanisms. This behavior can be distinguished from base diffusion length effects by careful analysis of the  $I$ - $V$  data.

The effects of impurities in n-base and p-base devices differ in degree but submit to the same modeling analysis. A comparison of calculated and measured performance for multiple impurities indicates a limited interaction between impurities, e.g., copper appears to improve titanium-doped cells.

### LIST OF SYMBOLS

$A$	Cell area, $\text{cm}^2$ .
$I$	Solar-cell terminal current, A.
$I_{sc}$	Short-circuited current, A.
$P$	Cell power, W.
$I_p$	Current at peak power point, A.

Manuscript received August 21, 1979; revised November 1, 1979. This work was performed as part of the Low Cost Solar Array Project and was sponsored by the Jet Propulsion Laboratory, California Institute of Technology, by agreement between the National Aeronautics and Space Administration and the U. S. Department of Energy.

J. R. Davis, Jr., A. Rohatgi, R. H. Hopkins, P. D. Blais, and P. Rai-Choudhury are with Westinghouse Research and Development Center, Pittsburgh, PA 15235.

J. R. McCormick and H. C. Mollenkopf are with Hemlock Semiconductor Corporation, Midland, MI.

$V_p$	Voltage at peak power point, V.
$n$	Ideality factor.
$R_s, R_{sh}$	Series and shunt resistances, $\Omega$ .
$I_0$	Diode saturation current, A.
$V_T$	$= kT/q$ , the thermal voltage, V.
$I_\lambda$	Photocurrent for illumination with wavelength $\lambda$ , A.
$L_\lambda$	$= 1/\alpha_\lambda$ , the absorption length at wavelength $\lambda$ , cm.
$R_\lambda$	Reflection coefficient at wavelength $\lambda$ .
$N_\lambda$	Number of photons at wavelength $\lambda$ , $\text{s}^{-1} \cdot \text{cm}^{-2}$ .
$x$	Distance from front surface of cell, cm.
$L_n, L_p$	Effective electron diffusion length, p base, n base.
$L_{n0}, L_{p0}$	Diffusion lengths in baseline cells.
$I_{sc0}$	Short-circuit current for baseline cells (no added impurities), A.
$I_n$	$= I_{sc}/I_{sc0}$ normalized short-circuit current.
$I_{n\infty}$	Value of $I_n$ which would result if $L_n$ were infinite.
$V_{oc0}$	Open-circuit voltage for baseline cells (no added impurities), V.
$V_n$	$= V_{oc}/V_{oc0}$ , normalized open-circuit voltage.
$V_{oc}$	Open-circuit voltage, V.
$N_x, N_y, N_z$	Concentration of impurity species $x, y$ , and $z$ , $\text{cm}^{-3}$ .
$\tau$	Minority-carrier lifetime.
$\tau_x$	Minority-carrier lifetime due to impurity $x$ .
$\tau_0$	Minority-carrier lifetime in baseline devices.
$\sigma_x$	Recombination cross section for impurity $x$ .
$v_{th}$	Thermal velocity.
$a_x$	Ratio of electrically active recombination centers to metallurgical concentration.
$k_x$	$= (\sigma_x v_{th} a_x)/D$ .
$C_1$	Model constant.
$C_{2x}$	Model constant specific to impurity $x$ .
$n_i$	Intrinsic carrier concentration, $\text{cm}^{-3}$ .

- $D, D_n, D_p$  Minority-carrier diffusivity,  $\text{cm}^2/\text{s}$ .  
 $i$   $= I/I_{sc0}$  normalized terminal current of the solar cell at voltage  $V$ .  
 $v$   $= V/V_{oc0}$  normalized terminal voltage at current  $I$ .

## I. INTRODUCTION

WE EXPECT impurities in silicon to influence solar-cell properties in a variety of ways. For example, crystal growth can be perturbed resulting in defects, inclusions, precipitates, or polycrystalline structure. The bulk properties of the silicon may be altered by electrically active impurity centers which reduce the minority-carrier diffusion length either by increased recombination or by scattering-induced mobility loss. Additionally, impurities may induce contact and contact interface degradation, series- or shunt-resistance effects, as well as precipitation and other junction defect mechanisms.

Our results, in nearly all cases, show that a reduction of the base diffusion length is the dominant mechanism of cell degradation. Notable exceptions are nickel, copper, and iron which at the higher concentrations result in substantial performance loss due to junction defect phenomena. None of the remaining effects mentioned were significant to cell performance.

The experimental characterization of impurity effects involved the introduction of controlled concentrations of selected impurities into the melt during crystal growth. The impurities selected comprised elements expected to be present in incompletely refined silicon or those which might be introduced later during silicon or cell processing: Al, B, C, Ca, Co, Cr, Cu, Fe, Mg, Mn, Mo, Nb, P, Pd, Ta, Ti, V, W, Zn, and Zr.

A first-order model was developed to predict the solar-cell performance as a function of the concentration of single impurity species. The model analysis described below was extended to multiple impurities, permitting examination of possible impurity interaction effects.

The data are in reasonable agreement with the theory and provide useful guidelines to those involved with the processing of silicon, growth of crystals, or the fabrication of solar cells.

## II. EXPERIMENTAL

### A. Crystal Growth

Ingots were prepared from Dow Corning semiconductor grade silicon by Czochralski pulling. Growth conditions were

pull rate	7 cm/h
seed rotation	10–15 r/min CW
crucible rotation	2–4 r/min CCW
charge weight	869 g (average)
ingot diameter	3.3 cm
atmosphere	1-atm argon.

The melts from which the crystals grew were co-doped with either boron or phosphorus and one or more elemental metals, typically 99.99 percent pure or better. The nominal resistivities were 0.3, 1, 4, and 30  $\Omega \cdot \text{cm}$  for the p-type crystals and 1  $\Omega \cdot \text{cm}$  for the n-type crystals.

TABLE I  
SEGREGATION COEFFICIENTS

Element	Effective Segregation Coefficient*
Al	$3 \times 10^{-2}$ ( $2.8 \times 10^{-3}$ )
B	0.8
C	0.05
Ca	?
Cu	$8.0 \times 10^{-4}$
Cr	$1.1 \times 10^{-5}$
Fe	$6.4 \times 10^{-6}$
Mg	$3.2 \times 10^{-6}$
Mn	$1.3 \times 10^{-5}$
Mo	$4.5 \times 10^{-8}$
Ni	$3.2 \times 10^{-5}$
P	0.35
Ta	$2.1 \times 10^{-8}$
Ti	$2.0 \times 10^{-6}$
V	$4 \times 10^{-6}$
Zn	$10^{-5}$
Zr	$< 1.5 \times 10^{-7}$
W	$1.7 \times 10^{-8}$
Co	$1.0 \times 10^{-5}$
Nb	$\sim 10^{-7}$

\*  $k_{\text{eff}}$  = ingot impurity concentration/melt impurity concentration

### B. Impurity Analysis

Precise and accurate determination of the ingot impurity concentrations poses a formidable task. The maximum melt concentration which could be achieved for the majority of elements studied was in the range of  $1 \times 10^{20}$  to  $4 \times 10^{20}$  atoms  $\cdot \text{cm}^{-3}$ . Higher melt concentrations resulted in polycrystalline ingot growth. This concentration limit coupled with the extremely small effective segregation coefficients [1]–[4] for many of the impurities (see Table I) produces ingot concentrations ranging from less than  $10^{12}$  atoms  $\cdot \text{cm}^{-3}$  to values as high as  $1 \times 10^{17}$  atoms  $\cdot \text{cm}^{-3}$ , corresponding to required detection limits of from 0.02 parts per billion to 2000 parts per billion. Only spark source mass spectroscopy and neutron activation analytical techniques are applicable to metal analysis in these ranges [3], [4]. Neutron activation analysis coupled with radiochemical separation and measurement provides the lowest detection limits, but the high costs and the relatively long times required precluded extensive use of this method.

The impurity concentration of each ingot  $C_s$  was measured by SSMS, NAA, or a combination of both methods, a vacuum cast sample was also collected from the residual melt of each growth run. This quenched material was analyzed by emission spectroscopy or atomic absorption to provide the melt impurity concentration  $C_L$ . Segregation coefficients ( $k = C_s/C_L$ ) determined for the most heavily doped ingots were used to calculate the ingot impurity concentration in cases where the ingot impurity level fell below the detection limits of the analytical methods. These analytic data were supplemented by deep-level transient spectroscopy (DLTS) which for some impurities has a detection limit below  $10^{-5}$  ppma [10]. Deep-level measurements were in good agreement with concentration data determined by the other methods.

Carbon and oxygen concentrations were measured by infrared absorption. The amplitude of the absorption peak for

carbon at  $606 \text{ cm}^{-1}$  and oxygen at  $1107 \text{ cm}^{-1}$  are proportional to the elemental concentrations. Constants of proportionality for this work were 2.2 for carbon and 9.6 for oxygen. In Czochralski ingots, carbon was found in the range from  $2.5 \times 10^{16}/\text{cm}^3$  to  $5 \times 10^{17}/\text{cm}^3$  and oxygen from  $5 \times 10^{17}/\text{cm}^3$  to  $1.5 \times 10^{18}/\text{cm}^3$ .

### C. Cell Fabrication

Solar cells were fabricated by a conventional process [2]–[4]. The pre-cleaned wafers were phosphorus diffused at  $850^\circ\text{C}$  for 50 min for  $n^+$ -p cells while  $p^+$ -n cells were boron diffused at  $875^\circ\text{C}$  for 30 min. This resulted in a junction depth of  $0.35 \mu\text{m}$  for both  $n$ - and  $p$ -base cells. The corresponding sheet resistances were 60 and  $90 \Omega/\text{square}$ . The cells with an area of  $1.03 \text{ cm}^2$  were mesa-etched and metallized with Ti-Pd-Ag using an electron-beam system. The front pattern was a five-finger grid with 5.4-percent area coverage.

Contacts were sintered at  $300$  to  $550^\circ\text{C}$  for 15 min in hydrogen. The efficiency of baseline cells (no added impurities) was  $(10.0 \pm 0.5)$  percent without antireflective coatings. With coatings the average efficiency was  $(14.1 \pm 0.7)$  percent. Efficiency variation in individual experiments was typically less by a factor of five. The usual experimental run consists of 15 to 25 wafers from the metal-doped ingots along with the 5 to 8 uncontaminated baseline wafers.

### D. Solar-Cell Characterization

Current-voltage measurements were made under illumination from a quartz-iodine simulator. The light level was set at  $91.6 \text{ mW}/\text{cm}^2$ , for the AM2 spectrum using a NASA-Lewis calibrated standard cell. The lighted  $I$ - $V$  data were interpreted by a computer program using a single-exponential model [2]–[4].

$$I = I_{sc} - I'_0 [\exp((V + IR_s)/nV_T) - 1]. \quad (1)$$

The fit gives the parameters  $I'_0$ ,  $R_s$ , and  $N$ . The peak power point ( $V_p$ ,  $I_p$ ) was determined by numerically solving the following equation:

$$dP/dI = I(dV/dI) + V = 0. \quad (2)$$

The cell efficiency was then determined by

$$\text{Eff} = (V_p \times I_p \times 100)/(91.6 \times A). \quad (3)$$

Additional cell data were obtained by measurement of carrier lifetimes using the open-circuit-voltage-decay (OCVD) and photoconductive-decay (PCD) methods. The relative effect of impurities on junction versus base properties of the cell was determined by dissecting the dark voltage-current characteristic into its two exponential components including series- and shunt-resistance effects [7]–[9].

## III. MODELING IMPURITY EFFECTS IN SILICON

The impurity effects model described in the following sections was derived to provide a means of predicting the performance behavior of solar cells made from silicon containing known concentrations of various impurities associated with silicon refining and processing.

Several key assumptions underlie the model formulation:

- The photovoltaic performance of the cell can be modeled as though the device consisted wholly of a single base region with uniform electrical properties.
- The effect of impurities is exclusively that of reducing the carrier diffusion length in the effective base region.
- The impurity-induced diffusion length reduction results either from carrier recombination via deep centers associated with the impurities or from carrier mobility loss due to ionized impurity scattering.
- The number of electrically active centers is a species-dependent linear function of the total metallurgical concentration of that impurity.

These assumptions imply the effective base diffusion length,  $L_n$ , is a characterizing parameter for the impurity effects. Experience has shown that the diffusion length, or, equivalently, the lifetime is difficult and time consuming to measure accurately. A simple reliable measurement is desirable because cell process variability requires a large amount of data to assure statistically meaningful results. We have, therefore, chosen to model the impurity effect as a function of the short-circuit current, a more easily measured quantity and one which is directly related to the diffusion length.

### A. Short-Circuit Current as a Function of Diffusion Length

A relationship between the photocurrent  $I_{sc}$  and the diffusion length  $L_n$  can be determined by solving the carrier transport equations with appropriate boundary conditions. A closed-form solution can be obtained for a single wavelength but for a real solar spectrum, a numerical integration is necessary. A one-dimensional computer solution for the AM2 spectrum is shown as the dashed curve in Fig. 1.

A closed-form expression would be more useful in constructing an impurity model so we examine the possibility of representing the distributed spectrum by an equivalent monochromatic illumination producing the same current in the cell. The differential equation for a single wavelength is

$$dI_\lambda = qA(N_\lambda/L_\lambda)(1 - R_\lambda) \exp(-x(1/L_\lambda + 1/L_n)) dx \quad (4)$$

where we assume the basewidth is large with respect to both the diffusion length  $L_n$  and the absorption length  $L_\lambda$ . The solution at a single wavelength is then

$$I_\lambda = \frac{qA(N_\lambda/L_\lambda)(1 - R_\lambda)}{[(1/L_\lambda) + (1/L_n)]} \cdot (1 - \exp(-x(1/L_\lambda + 1/L_n))). \quad (5)$$

The effective base thickness for a diffusion length limited cell, without a back surface field, is on the order of two diffusion lengths so let  $x = 2L_n$ .

For a wavelength near the middle of the solar spectrum the absorption length  $L_\lambda \approx 20 \mu\text{m}$  and we obtain

$$I_\lambda = I_{sc} \approx qAN_\lambda(1 - R_\lambda)/(L_\lambda/L_n + 1) \cdot (1 - \exp(-2L_n/20 - 2)). \quad (6)$$

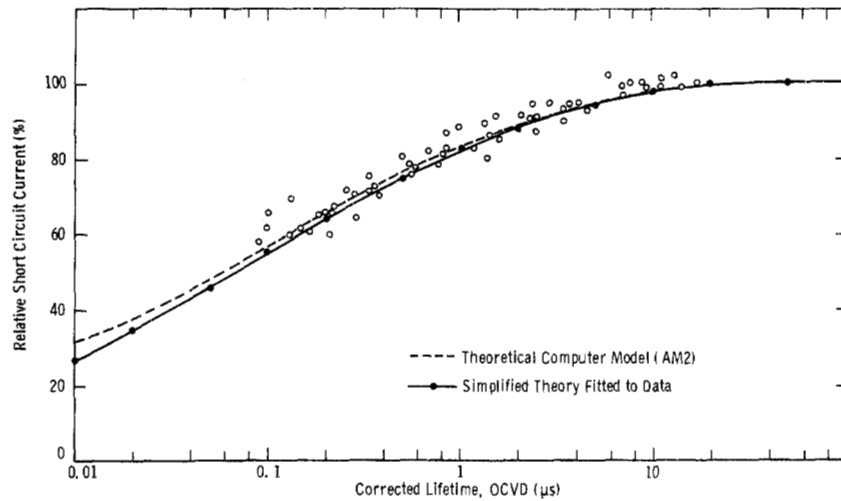


Fig. 1. Photocurrent as a function of lifetime.

Over the range of values of  $L_n$  appropriate to our experiments the second term is essentially unity and we have

$$I_{sc} \doteq \frac{qAN_\lambda(1 - R_\lambda)}{(L_\lambda/L_n) + 1}. \quad (7)$$

Defining normalized variables

$$I_{sc0} = I_{sc} \text{ (baseline sample)}$$

$$I_n = \frac{I_{sc} \text{ (impurity sample)}}{I_{sc0}}$$

$$I_{n\infty} = \frac{I_{sc}(L_n = \infty)}{I_{sc0}} = \frac{qAN_\lambda(1 - R_\lambda)}{I_{sc0}}.$$

Equation (7) becomes the convenient form

$$I_n = I_{n\infty} \left( \frac{1}{(L_\lambda/L_n) + 1} \right). \quad (8)$$

A least squares fit of (8) to experimental data provides the values shown in Fig. 1;  $I_{n\infty} = 1.11$  and  $L_\lambda = 19.2 \mu\text{m}$ . An absorption length of  $19.2 \mu\text{m}$  corresponds to a wavelength of 860 nm which is plausibly near the center of the solar spectrum. The data scatter is largely a result of inaccuracies in the open-circuit decay lifetime measurement.  $L_{n\infty}$  and  $L_\lambda$  are model constants which depend only on device geometry, primarily the cell thickness.

### B. Impurity-Dependent Diffusion Length

The diffusion length within the cells depends on the density of recombination centers. We assume no concentration-dependent effects and thus expect the density of centers  $N_T$  to be proportional to the total concentration of the metal impurity atoms  $N_x$ . Note that  $N_T$  need not equal  $N_x$  since many metal atoms may be in electrically inactive sites, e.g., due to precipitation.

The lifetime as a function of  $N_T$  under low-level injection can be approximated by

$$\tau = 1/(\sigma_x v_{th} N_T) \quad (9)$$

where  $\sigma_x$  is the recombination cross section for metal  $x$  and  $v_{th}$  is the thermal velocity of the carriers. Let  $N_T = a_x N_x$ ; where  $a_x$  is the assumed proportionality constant.

$$\tau = 1/(\sigma_x v_{th} a_x N_x). \quad (10)$$

With several independent lifetimes, the effective lifetime is obtained from the reciprocal sum

$$\frac{1}{\tau} = \frac{1}{\tau_0} + \frac{1}{\tau_x} + \dots + \frac{1}{\tau_z} \quad (11)$$

where  $\tau_0$  is lifetime observed in uncontaminated baseline samples and  $\tau_x$ ,  $\tau_y$ , and  $\tau_z$  are associated with the metals  $x$ ,  $y$ ,  $\dots$ , and  $z$ . Using the relationship  $L_n^2 = D_n \tau$  with (10) and (11) gives

$$1/L_n^2 = 1/L_{n0}^2 + k_x N_x + k_y N_y + \dots + k_z N_z \quad (12)$$

where

$$k_x = \frac{\sigma_x v_{th} a_x}{D_n}.$$

Equation (8) then takes the following convenient form:

$$(I_{n\infty}/I_n - 1)^2 = L_\lambda^2 [1/L_{n0}^2 + k_x N_x + k_y N_y + \dots + k_z N_z]. \quad (13)$$

For samples containing single metal impurities, (13) becomes

$$\left( \frac{I_{n\infty}}{I_n} - 1 \right)^2 = \frac{L_\lambda^2}{L_{n0}^2} + L_\lambda^2 k_x N_x. \quad (14)$$

Defining constants  $C_1$  and  $C_{2x}$  we have

$$\left( \frac{I_{n\infty}}{I_n} - 1 \right)^2 = C_1 + C_{2x} N_x. \quad (15)$$

The constants  $C_1$  and  $C_{2x}$  are then determined by fitting (15) to the experimental data. Equation (15) may also be expressed in a useful alternate form

$$\begin{aligned} \left( \frac{I_{n\infty}}{I_n} - 1 \right)^2 &= C_1 \left( 1 + \frac{C_{2x}}{C_1} N_x \right) \\ &= C_1 \left( 1 + \frac{N_x}{N_{0x}} \right) \end{aligned} \quad (16)$$

TABLE II  
MODEL COEFFICIENTS FOR SINGLY DOPED, p-BASE SOLAR CELLS

IMPURITY	$C_1$	$C_{2X}$	$N_{OX}$
Aluminum	1.2 E-02	2.9 E-18	4.4 E+15
Chromium	9.2 E-03	6.7 E-17	1.3 E+14
Copper	1.2 E-02	3.0 E-20	4.1 E+17
Iron	1.2 E-02	4.7 E-17	2.5 E+14
Manganese	9.8 E-03	5.3 E-17	1.8 E+14
Molybdenum	1.3 E-02	2.0 E-14	6.0 E+11
Nickel	1.4 E-02	2.5 E-18	5.0 E+15
Phosphorous	1.1 E-02	6.8 E-21	1.7 E+18
Tantalum	1.2 E-02	5.1 E-14	2.3 E+11
Titanium	1.2 E-02	4.5 E-15	2.6 E+12
Vanadium	1.3 E-02	5.4 E-13	2.5 E+12
Zirconium	1.0 E-02	2.7 E-14	3.6 E+11
Tungsten	1.1 E-02	9.1 E-15	1.2 E+12
Cobalt	1.2 E-02	1.0 E-17	1.1 E+15
Niobium	1.2 E-02	7.4 E-15	1.6 E+12

TABLE III  
MODEL COEFFICIENTS FOR SINGLY DOPED, n-BASE SOLAR CELLS

IMPURITY	$C_1$	$C_{2X}$	$N_{OX}$
Aluminum	1.0 E-02	1.1 E-18	8.5 E+16
Chromium	1.0 E-02	8.7 E-17	1.2 E+14
Copper	1.1 E-02	1.3 E-19	8.0 E+16
Iron	1.0 E-02	5.7 E-17	1.8 E+14
Manganese	1.1 E-02	1.2 E-17	9.5 E+14
Titanium	1.3 E-02	3.6 E-16	3.7 E+13
Vanadium	1.3 E-02	3.3 E-16	4.1 E+13
Molybdenum	1.1 E-02	8.5 E-15	1.3 E+12

where we have defined  $N_{0x} = C_1/C_{2x}$ , a threshold concentration for impurity  $x$  above which cell performance is degraded. The value of  $I_n$  for  $N_x = N_{0x}$  depends on  $I_{n\infty}$

$$I_n(N_{0x}) = \frac{I_{n\infty}}{I_{n\infty}\sqrt{2} + (1 - \sqrt{2})}. \quad (17)$$

$I_n(N_{0x})$  is approximately 0.97 for the data shown in Tables II and III in which the constants of (14) and (15) were obtained by the least squares fit to experimental data for solar cells doped with an impurity.

### C. Open-Circuit Voltage Behavior

Following the diffusion-controlled model the normalized open-circuit voltage is given by

$$V_n = \frac{nV_T}{V_{oc0}} \ln \left( \frac{I_{sc}}{I_0} \right). \quad (18)$$

This expression derives from the “shifting approximation” [5] which requires that the space-charge region contribute little to either the photocurrent or the dark current and that low-level injection conditions are maintained. These constraints are generally satisfied for the experimental devices used in this study.

Assuming a p-base cell, the saturation current is approximately that originating in the base region

$$I_0 = \frac{qAn_i^2 D_n}{N_A L_n}. \quad (19)$$

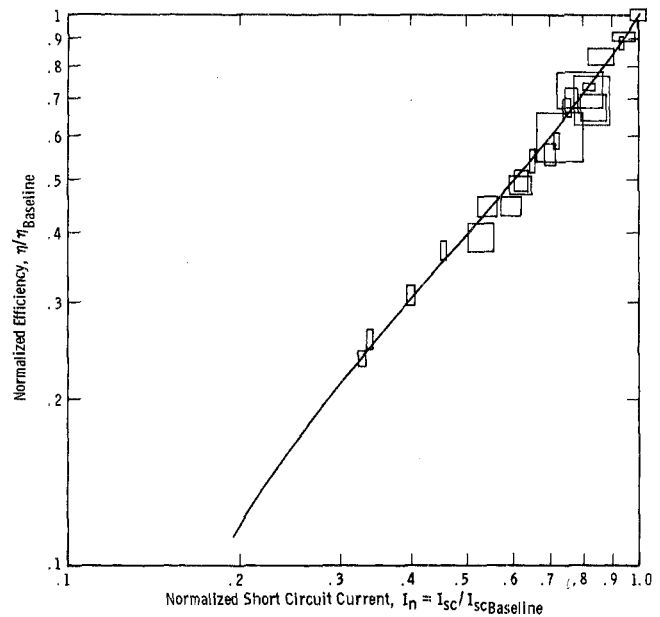


Fig. 2. Open-circuit voltage as function of short-circuit current for metal-doped solar cells.

Obtaining  $L_n$  from (8),  $I_0$  can be written in terms of the short-circuit current

$$I_0 = \frac{qAn_i^2 D_n}{N_A} \frac{I_{n\infty}}{L_\lambda} \left( \frac{1}{I_n} - \frac{1}{I_{n\infty}} \right). \quad (20)$$

Combining (20) and (18) gives the desired relationship between  $V_n$  and  $I_n$

$$V_n = \frac{nV_T}{V_{oc0}} \ln \left( \frac{N_A L_\lambda I_{sc0}}{qAn_i^2 D_n I_{n\infty}} \right) + \frac{nV_T}{V_{oc0}} \ln \left( \frac{I_n}{(1/I_n) - (1/I_{n\infty})} \right) \quad (21)$$

which may be written in the form

$$V_n = E \ln \left( \frac{I_n}{(1/I_n) - (1/I_{n\infty})} \right) + F. \quad (22)$$

A least squares fit of (22) to experimental data for  $4\text{-}\Omega \cdot \text{cm}$  p-base devices is shown in Fig. 2 and provides  $E = 0.0472$  and  $F = 0.8747$ .

Direct calculation gives  $E = 0.0477$  and  $F = 0.8740$  where  $N_A = 3.5 \times 10^{15} \text{ cm}^{-3}$ ,  $D_n = 32 \text{ cm}^2/\text{s}$ ,  $L_\lambda = 0.0019 \text{ cm}$ ,  $I_{sc0} = 0.0225 \text{ A}$ ,  $A = 1 \text{ cm}^2$ ,  $V_{oc0} = 0.556 \text{ V}$ ,  $I_{n\infty}$  and  $L_\lambda$  are deduced from the experimental data, the remaining values are measured. Note that the voltage behavior, unlike short-circuit current, is dependent on the base doping.

### D. Efficiency Behavior

To relate efficiency to short-circuit current, we again rely on the “shifting approximation” [5] to provide the illuminated voltage-current equation

$$I = I_{sc} - I_0 \exp \left( \frac{V}{nV_T} \right). \quad (23)$$



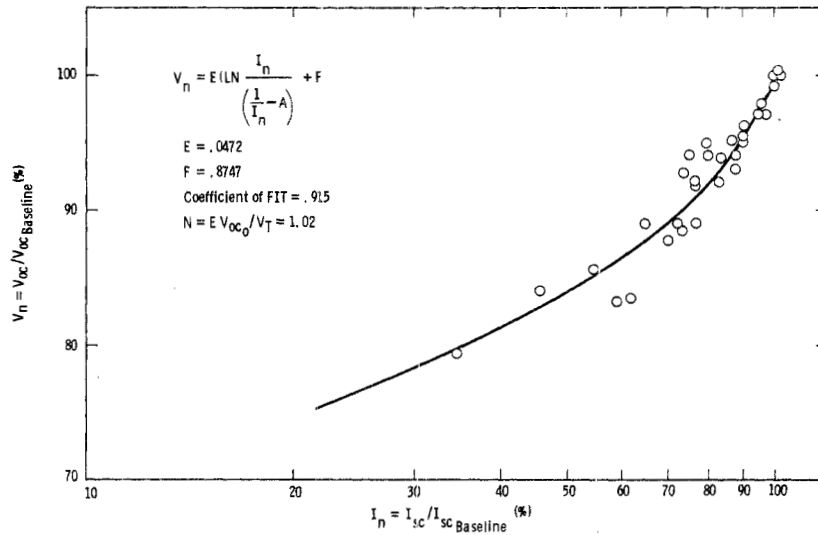


Fig. 3. Efficiency as a function of short-circuit current.

Substituting from (20) for  $I_0$  and normalizing the voltages and currents gives

$$i = I_n - \frac{qAn_i^2 D_n I_{n\infty}}{N_A L_{\lambda} I_{sc0}} \left( \frac{1}{I_n} - \frac{1}{I_{n\infty}} \right) \exp \left( \frac{v V_{oc0}}{n V_T} \right). \quad (24)$$

Using the data given in Section III-C the coefficient of the second term is  $9.58 \times 10^{-9}$ . Applying the boundary constraint that if  $I_n = 1$  and  $i = 0$  then  $v = 1$  leads to a value for  $n = 1.0151$  which agrees with the value obtained in the  $V_{oc}$  analysis.

The normalized peak power is obtained from the cell when

$$\frac{dp}{dv} = \frac{d(iv)}{dv} = i + v \frac{di}{dv} = 0. \quad (25)$$

This combined with (24) becomes

$$I_n - \left( \frac{qAn_i^2 D_n I_{n\infty}}{N_A L_{\lambda} I_{sc0}} \right) \left( \frac{1}{I_n} - \frac{1}{I_{n\infty}} \right) \exp \left( \frac{v V_{oc0}}{n V_T} \right) \cdot \left( 1 + \frac{v V_{oc0}}{n V_T} \right) = 0. \quad (26)$$

Numerically solving (26) for the peak power voltage  $v_p$  and (24) for  $i_p$  with  $I_n$  as a parameter provides the normalized efficiency where the zero subscripts denote baseline values.

$$\frac{\eta}{\eta_0} = \frac{i_p v_p}{i_{p0} v_{p0}}. \quad (27)$$

The resulting curve of  $\eta/\eta_0$  as a function of  $I_n$  shown in Fig. 3 is in good agreement with experimental data. As (26) has no closed-form solution, an empirical approximation was obtained.

$$\frac{\eta}{\eta_0} = 0.872 I_n^{1.128} + 0.128 I_n^{12}. \quad (28)$$

#### E. Single Impurity Behavior

The efficiency as a function of metal concentrations can now be calculated using (13) or (15) with the coefficients given in Table II to obtain  $I_n$  and (28) then provides the efficiency.

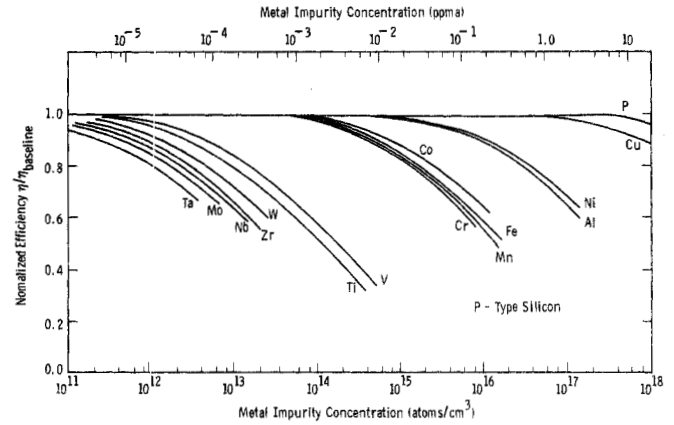


Fig. 4. Solar-cell efficiency versus impurity concentration for 4-Ω · cm p-base devices.

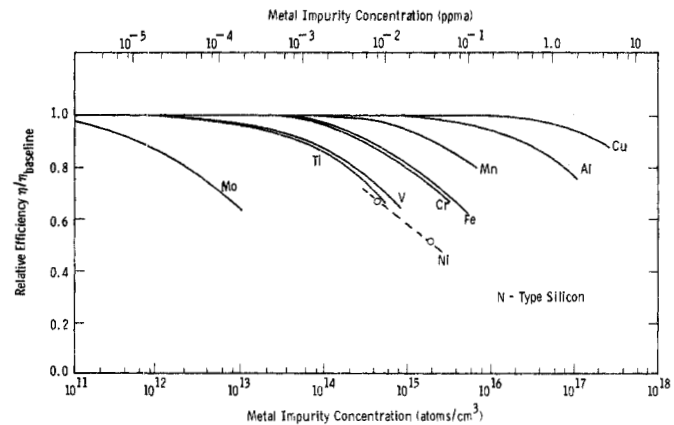


Fig. 5. Solar-cell efficiency versus impurity concentration for 1.5-Ω · cm n-base devices.

Nearly 200 impurity containing ingots were processed into solar cells and the data analyzed by this method were used to compute the least squares coefficients listed in Tables II and III and to derive the curves depicted in Figs. 4 and 5. These results for 4-cm p-base and 1-Ω · cm n-base devices are com-

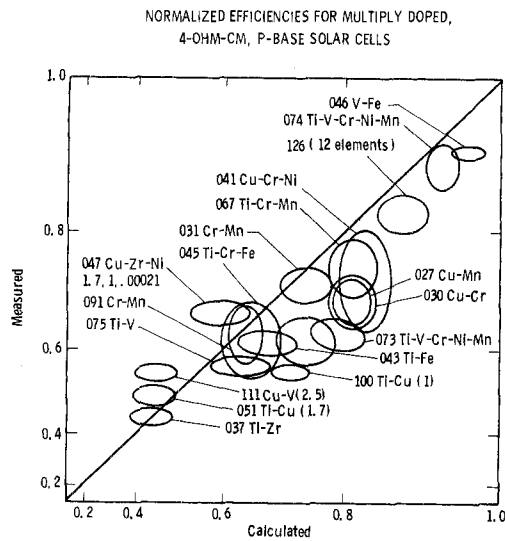


Fig. 6. Comparison of impurity threshold concentration ( $N_{0x}$ ) for cell degradation in n- and p-base solar cells.

pared in Fig. 6. Of particular interest is the fact that n-base devices are generally less affected by several impurities than are the corresponding p-base devices. In this figure, a larger value of  $N_{0x}$  implies a reduced degradation sensitivity to impurity  $x$ .

Experimental data have been omitted for clarity from Figs. 4 and 5 but the agreement with the model curves is quite good [3], [4]. Notable exceptions are for iron, copper, and nickel which at their highest concentrations induce excessive junction shunting and depletion-region recombination. These mechanisms were excluded from the model analysis because of their unpredictable behavior. An example of junction degradation by copper is shown in Fig. 7. The dark  $I$ - $V$  data are shown as the two exponential components governing the diffusion current (upper right) and the junction depletion current (bottom left) [2], [6], [7]. The effects of series and shunt resistance have been removed [8], [9]. It is apparent that the upper segment shifts little with increasing copper concentration reflecting negligible change in the base lifetime.

The shift of the lower segments, however, implies a considerable current increase which accounts for nearly all of the cell degradation. This excess junction current is thought to be mainly due to a combination of nonlinear shunting and field emission associated with precipitates rather than simple recombination in the depletion layer.

The dissected dark  $I$ - $V$  data for titanium containing devices, shown in Fig. 8, show the dominant effect to be a loss of bulk lifetime evidenced by the shift of the upper curves to the left with increasing Ti concentration. The depletion-region component of the dark current, denoted by the lower segments, shows some increase with the higher Ti concentrations but remains negligible with respect to device performance.

#### F. Multiple Impurity Results

Having determined the model constants for single impurities, the linearity of (13) permits calculating the expected performance of samples containing multiple impurities. The calculation includes the assumption that the impurities act inde-

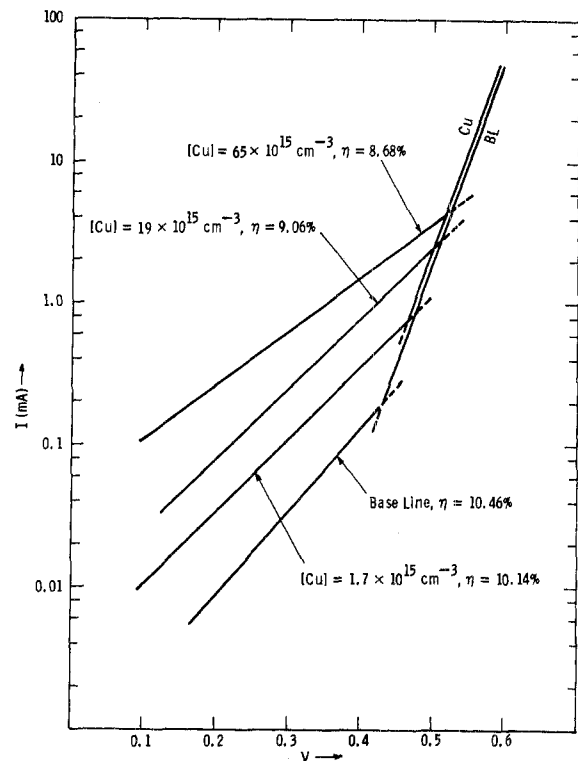


Fig. 7. Transformed dark  $I$ - $V$  characteristics for 4- $\Omega \cdot \text{cm}$  Cu-doped silicon solar cells.

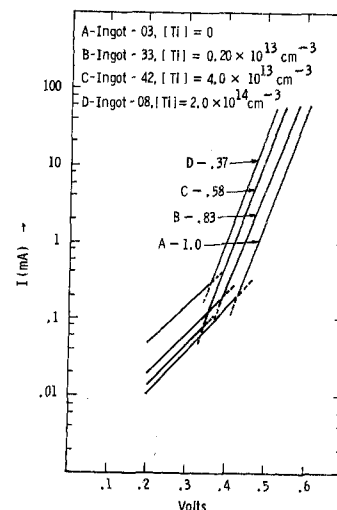


Fig. 8. Transformed dark  $I$ - $V$  characteristics for 4- $\Omega \cdot \text{cm}$  Ti-doped silicon cells. Curves are labeled with normalized cell efficiencies.

pendently, thus a comparison of calculated and experimental values permits assessment of any interactive effects. Such a comparison is shown in Fig. 9 for the multiply doped samples identified in Table IV. These data suggest a general anti-synergic behavior evidenced by the calculated efficiency being larger than the measured value, i.e., the points lie below the unity slope correlation line. However, supplementary data obtained by the dark  $I$ - $V$  analysis and DLTS have shown negligible impurity interactivity except for copper with titanium, vanadium, and zirconium. The general downward displacement of the data is usually due either to junction degradation

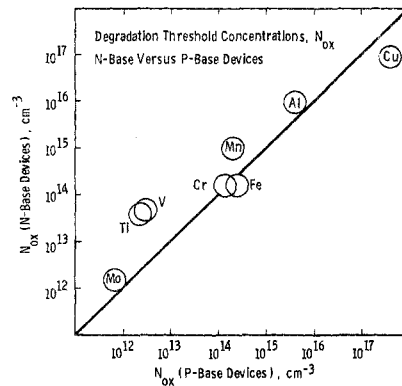


Fig. 9. Normalized efficiencies for multiply doped  $4\text{-}\Omega \cdot \text{cm}$  p-base solar cells.

TABLE IV  
IMPURITY CONCENTRATIONS FOR MULTIPLY DOPED INGOTS  
( $10^{15}$  atoms  $\cdot \text{cm}^{-3}$ )

Ingot No.	Ti	Cu	V	Cr	Fe	Zr	Ni	Mn
027		1.7						1.3
030		1.7		1.0				
031				1.0				1.3
037	0.22					<0.0007		
041		1.7		0.8			2.1	
043	0.033				0.56			
045	0.039			0.65	0.43			
046			0.07		0.57			
047		1.7				<0.00021	1.0	
050	0.0002		0.0004					
051	0.20	1.7						
061	0.011			1.0				
067	0.0033			0.4				0.5
073	0.0024		0.004	0.4			2.0	0.4
074	0.00033		0.0006	0.08			0.5	0.08
091				0.5				0.3
100	0.033	1.0						
111		2.5	.3					
126	Al, 1.0; B 3.5; Cr .02; Cu .80; Fe .02, Mn .02; Mo .00015; Ni .80; P .9; Ti .0004; V .0004; Zr .0004							
75	.056		.1					
104	.14	2.0						
162	.2						1.21	
185	.15	1.2						

effects not included in the calculations or to inaccurate impurity concentration data.

In the case of Ti, V, and Zr, the addition of copper results in a small improvement in cell performance. DLTS measurements, in fact, have shown that the number of recombination centers due to these impurities is reduced by copper. It is believed that the mobile copper atoms diffuse to the locations of the second metal species, where co-precipitation then electrically deactivates some of the Ti, V, or Zr.

#### G. Polycrystalline Behavior and Resistivity Effects

We have examined the effects of a number of impurities in samples with resistivities ranging from  $0.2$  to  $30 \Omega \cdot \text{cm}$  and in polycrystalline material produced by Czochralski growth.

A convenient way of presenting these results is by determining the impurity concentration threshold  $N_{0x}$  and comparing the experimental value to that deduced from the  $4 \Omega \cdot \text{cm}$  single-crystal data. Using subscripts  $\alpha$  and  $\beta$  to designate  $4\text{-}\Omega \cdot \text{cm}$  p-base and the comparison sample data, respectively, we obtain from (8) and (16), the experimental threshold  $N_{0x\beta}$ . All currents are normalized with respect to the  $\alpha$  baseline

values

$$N_{0x\beta} = \frac{N_{x\beta}}{\left( \frac{(I_{n\infty}/I_{n0\beta}) - 1}{(I_{n\infty}/I_{n0\alpha}) - 1} \right)^2 - 1} \quad (29)$$

$I_{n\beta}$  is the normalized short-circuit current in the cell containing impurity  $x$  at a concentration of  $N_{x\beta}$ .  $I_{n0\beta}$  is the current measured in  $\beta$  samples containing no added impurities.

If we assume the impurities behave identically in  $4\text{-}\Omega \cdot \text{cm}$  p-base samples and in the  $\beta$  samples we can deduce a value for  $N_{0x\beta}$ . After some manipulation of the equations, we obtain for the expected value of the degradation threshold

$$N_{0x\beta} = \frac{D_{n\beta} [(I_{n\infty}/I_{n0\beta}) - 1]^2}{D_{n\alpha} C_{2x}} \quad (30)$$

Data expressed in this manner are shown in Fig. 10 for the devices described in Table V. Quantities given in parentheses are present in the baseline samples in which  $I_{n0\beta}$  is measured. These data show that for most of cases considered the impurity degradation effects can be projected from the behavior in the  $4\text{-}\Omega \cdot \text{cm}$  p-base devices. The data for ingot 148, as ex-



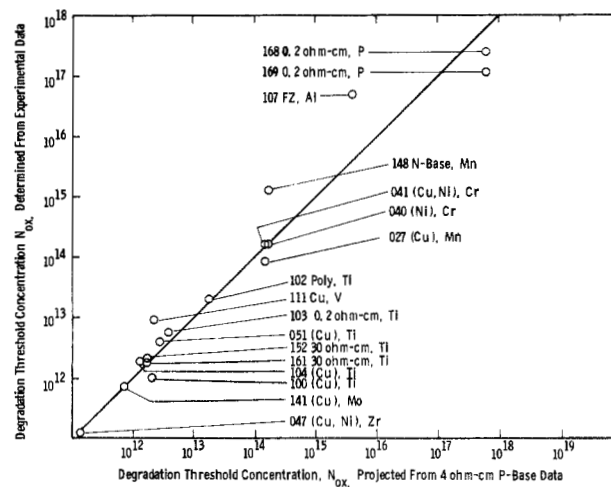


Fig. 10. Cell degradation thresholds obtained from measurements compared to thresholds projected from 4- $\Omega \cdot \text{cm}$  p-base data.

TABLE V  
SAMPLE DATA FOR DEGRADATION THRESHOLD COMPARISONS OF FIG. 10

Ingot	Resistivity ohm-cm	Type	Cr	Cu	Impurity Concentration $\times 10^{15} \text{ cm}^{-3}$							$I_{\text{sc08}}$ mA	$I_{\text{n8}}$	$I_{\text{no8}}$
					Mn	Mo	Ni	P	Ti	V	Zr			
041	4	P	.80	(1.7)			(3.0)					22.9	.843	1.018
047	4	P		(1.7)			(.75)				.0015	22.9	.955	1.018
051	4	P		(1.5)					.20			22.5	.614	1.000
100	4	P		(1.0)					.033			22.7	.695	1.009
102 poly	4	P							.11			19.2	.606	.860
103	.22	P							.17			20.4	.517	.907
104	4	P		(2.0)					.167			23.1	.649	1.029
111	4	P		(2.5)						.30		22.5	.579	1.000
141	4	P		(4.0)		.004						22.5	.832	1.000
148	2	N			.60							22.42	.929	.996
152	30	P							.021			22.41	.687	.996
161	30	P							.020			22.41	.838	.996
168	.22	P						110+				22.03	.950	.979
169	.22	P						136+				21.93	.942	.975

pected, have a higher measured threshold since manganese produces less effective recombination centers in n-base than in p-base silicon.

It can also be seen that the presence of copper increases the threshold slightly for titanium and vanadium. Data for ingot 100 are anomalous; it is thought that the titanium concentration is actually higher by a factor of three than the value quoted. Titanium in polycrystalline cells (ingot 102) acts almost identically as in single-crystal devices, a result which has been corroborated by DLTS measurements.

The high- and low-resistivity data agree with the projection with low-resistivity devices being slightly less affected.

Ingots 168 and 169 are heavily compensated with phosphorus and showed considerable longitudinal variation in resistivity because of the difference in segregation between boron and phosphorus. As a consequence, the cell data had considerable scatter. It is apparent that the tolerance for phosphorus is sufficiently high that problems will be experienced in controlling ingot resistivity before cell degradation due to compensation occurs.

#### H. Deep-Level Analysis

Nearly all the impurities in this study act as carrier recombination centers. These centers were examined by the method of DLTS [10], [11] which provided a sensitive method of impurity analysis and a means of determining the energy density and capture rates of impurity-induced active centers. We can, therefore, determine the fraction of total metallurgical concentration that becomes electrically active. Data in Fig. 11 show this ratio to be a specie-dependent constant as assumed in the model analysis. These data were obtained using Schottky diodes with both n-base and p-base samples as well as with samples containing multiple impurities. These results indicate negligible impurity or doping interaction.

Our use of Schottky barriers without optical injection although minimizing processing effects restricts the obtainable data to properties of majority-carrier traps.

Furthermore, while DLTS provides majority-carrier capture cross sections, there is no necessary relationship to the minority cross section which controls solar-cell performance. We

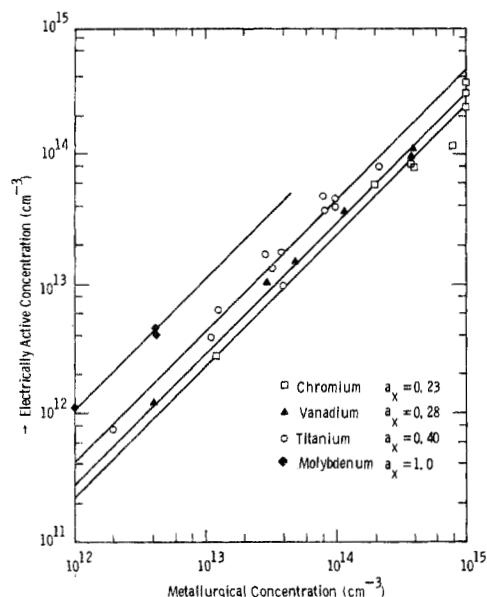


Fig. 11. Measured electrically active deep-level concentrations versus the metallurgical concentrations for several metal impurities.

can, however, deduce the effective recombination cross sections for minority carriers from the measured  $N_T/N_x$  ratios ( $a_x$ ) and the values of  $C_{2x}$  obtained from the solar-cell data (Tables II and III).  $C_{2x}$ , as defined in (12) and (15), permits expressing the cross section as

$$\sigma_x = \frac{D_n C_{2x}}{L_n^2 v_{th} a_x} \quad (31)$$

The resulting values are given in Table VI. The cross sections and the  $N_T/N_x$  ratios are subject to the same uncertainty as are the values of  $N_x$  which are considered correct within a factor of about two.

#### IV. CONCLUSIONS

We have studied the effects of various elemental impurities, both singly and in combinations, on the performance of silicon solar cells. Czochralski and polycrystalline ingots were employed with boron and phosphorus as primary dopants and with controlled additions of the secondary impurities.

These crystals and solar cells made from them were examined by a variety of chemical, analytical, structural, and electrical measurement techniques to provide a detailed and internally consistent description of the relationships between the impurity concentrations and the solar-cell performance.

The data obtained from over 200 crystals indicated that impurity-induced performance loss is primarily due to a reduction of the base diffusion length. Based on this observation, a model was developed which predicts cell performance as a function of secondary impurity concentrations. By including the effective segregation coefficients, the model may be used to predict cell performance from the impurity concentrations in the silicon feedstock used for crystal growth. The model calculations are in good agreement with experimental values except for Cu, Ni, Fe, and to a lesser degree,

TABLE VI  
MEASURED TRAP PROPERTIES FOR IMPURITIES IN SILICON

Elements	Majority Trap Energy (eV)	$N_T/N_x$ ( $a_x$ )	Effective Minority Carrier Recombination Cross Sections	
			$\sigma_n$	$\sigma_p$
Al	$E_V + 0.43 \pm .05$ $E_V + 0.47 \pm .03$	$1.9 \times 10^{-4}$	$1.4 \times 10^{-14}$	$5.7 \times 10^{-15}$
Cr	$E_V + 0.22 \pm .01$ $E_V + 0.31 \pm .02$ $E_C - 0.25 \pm .01$	0.23	$2.66 \times 10^{-16}$	$3.5 \times 10^{-16}$
Cu	---	---	---	---
Fe	$E_V + 0.40 \pm .04$	---	---	---
Mn	$E_V + 0.40 \pm .02$	---	---	---
Mo	$E_V + 0.30 \pm .01$	1.0	$1.85 \times 10^{-14}$	$7.8 \times 10^{-15}$
Ni	---	---	---	---
Ta	---	0.8 *	$5.9 \times 10^{-14}$ *	---
Ti	$E_V + 0.30 \pm .02$ $E_C - 0.26 \pm .02$	0.4	$1.04 \times 10^{-14}$	$8.3 \times 10^{-16}$
V	$E_V + 0.42 \pm .02$ $E_C - 0.22 \pm .01$ $E_C - 0.46 \pm .02$	0.28	$1.77 \times 10^{-14}$	$1.1 \times 10^{-15}$
Nb	$E_V + 0.12 \pm .02$	.19	$3.6 \times 10^{-14}$	---
W	---	---	---	---

\* Tentative Data

carbon, which at high concentrations induce structural defects and precipitation effects and degrade the cells mainly by erratic junction defect mechanisms as opposed to the more usual base diffusion length loss.

The impurity effects in samples containing single and multiple impurities, Czochralski, polycrystals, n base, high and low resistivity are self-consistent with the following exceptions: the presence of copper slightly reduces the degradation of Ti and V; n-base devices are less sensitive to many of the most harmful impurities.

The data provided by this study and the modeling of the solar cell performance impurity relationships make it possible to do tradeoff analyses at various stages of the manufacture of solar cells from the silicon feedstock to the finished product. A specification of an acceptable impurity content for solar cells depends on the acceptable cell efficiency, the crystal growth methodology, and the cell design and fabrication technology. However, it appears improbable that feedstock impurity concentrations above one part per million for elements like Mo or Ti or 100 parts per million for more benign impurities like Ni will be tolerable, even for crystal-growth methods like Czochralski or silicon web which exert large melt segregation effects.

#### ACKNOWLEDGMENT

The authors would like to thank the following individuals whose contributions have been important to the success of this effort: D. N. Schmidt (cell processing and testing), B. F. Westwood (process experiments and photolithography), A. M. Stewart (material characterization), H. F. Abt (metallization), C. F. Seiler (device measurements), S. Karako (DLTS measurements), T. Zigarovich (mask preparation), and M. C. Santoro and M. Thomas (manuscript preparation).

## REFERENCES

- [1] R. H. Hopkins *et al.*, *J. Crystal Growth*, vol. 42, p. 43, 1977.
- [2] J. R. Davis *et al.*, "Characterization of the effects of metallic on silicon solar cells," in *Proc. 13th IEEE Photovoltaic Specialists Conf.*, p. 490, 1978.
- [3] R. H. Hopkins *et al.*, 11th Quarterly Rep. and Summary, Silicon Materials Task (Part 2), DOE/JPL Tech. Rep. 954331-78/3, July 1978.
- [4] R. H. Hopkins *et al.*, 5th Quarterly Rep. and Summary, Silicon Materials Task (Part 2), DOE/JPL Tech. Rep. 954331-77/1, Jan. 1977.
- [5] F. A. Lindholm, "Application of the superposition principle to solar cell analysis," *IEEE Trans. Electron Devices*, vol. ED-26, p. 165, 1979.
- [6] A. Rohatgi *et al.*, "Effect of titanium, copper and iron on silicon solar cells," to be published in *J. Solid-State Electron.*
- [7] A. Neugroschel, F. Lindholm, and C. T. Sah, "A method for determining the emitter and base lifetime in p-n junction diodes," *IEEE Trans. Electron Devices*, vol. ED-24, p. 662, 1977.
- [8] R. J. Stirn, "Junction characteristics of silicon solar cells," in *Proc. 9th IEEE Photovoltaic Specialists Conf.*, p. 72, 1972.
- [9] M. Wolfe and H. Rauschenbach, "Series resistance effects on solar cell measurements," in *Solar Cells*, C. E. Backus, Ed. New York: IEEE Press, 1976, p. 89.
- [10] G. L. Miller, D. V. Lang, and L. C. Kimerling, "Capacitance transient spectroscopy," *Ann. Rev. Mat. Sci.*, p. 377, 1977.
- [11] D. V. Lang, "Deep level transient spectroscopy: A new method to characterize traps in semiconductors," *J. Appl. Phys.*, vol. 45, p. 3023, 1974.

# Grain Boundary Effects on the Electrical Behavior of Al-Poly-Si Schottky-Barrier Solar Cells

CHII-MING M. WU, MEMBER, IEEE, EDWARD S. YANG, SENIOR MEMBER, IEEE, W. HWANG, AND  
HOWARD C. CARD, MEMBER, IEEE

**Abstract**—Schottky-barrier diodes using aluminum on p-type polycrystalline silicon have been fabricated. The contrast of the orientation of neighboring grains is observed after chemical etching of the surface. Comparing the surface morphology of the substrate with the electronic behavior of the Schottky diode, we are able to identify the influence of grain boundaries. It is found that the low-angle boundary has little effect on the  $I$ - $V$  characteristics since near ideal Schottky  $I$ - $V$  curves are obtained. The barrier height is calculated to be 0.83 V which is higher than that of the single-crystal substrate. The ideality factor is 1.17 for a device containing a twin and low-angle boundaries. The high-angle grain boundary, however, significantly alters both the  $I$ - $V$  and low-frequency  $C$ - $V$  plots. The experimental data indicate that recombination centers and traps are introduced, resulting in an increase in recombination current and a reduction of the effective mobility. The conduction mechanisms for the two types of diodes are clearly distinguishable both in the dark and under illumination. In the photovoltaic operation under a tungsten lamp, we obtain an open-circuit voltage of 0.48 V and a fill factor 0.51. It appears that the chemical etching along with Schottky-barrier fabrication will provide a useful method to study the polycrystalline substrate for low-cost solar cell applications.

## INTRODUCTION

IT IS NOW apparent that polycrystalline silicon (poly-Si) is one of the most promising materials toward the realization of low-cost solar cells for terrestrial applications. To be able to utilize the polycrystalline materials, we must understand the

physics of the grain boundaries so that their influence on the photovoltaic properties of the solar cell may be assessed. Recently, theoretical models of the grain boundaries have been made by various workers for the electronic processes in the dark and under illumination [1]–[5]. At the same time, experimental investigations have been performed using the MIS structure [6]–[8], and an efficiency of 17.6 percent has been reported [9]. These experimental articles, however, do not relate the electrical and photovoltaic behaviors to the structural features of the substrate. In other words, the impact of grain boundaries has been treated as an integral part of the device without being specific. In this paper, we focus our attention on the influence of grain boundaries on the experimental electrical behavior of Al-poly-Si Schottky barriers on Wacker wafers. Our purpose is two-fold. First, the Schottky barrier may be used as an experimental tool to investigate the nature of the grain boundaries. Second, Schottky-barrier solar cells using MIS and MS structures may present the best way to reduce costs in device fabrication.

In this work, we compare devices fabricated on the *same substrate* in which different grain boundary angles are observed. The structural and electrical characteristics are correlated so as to deduce the influence of the grain boundary. We have also investigated the effect of surface etching of the as-sawn Wacker wafers, which modifies the electron properties of the junction. Both  $I$ - $V$  and  $C$ - $V$  measurements are made, and the frequency dependence of the  $C$ - $V$  curve is studied. The barrier height is calculated, and the open-circuit voltage is determined.

Manuscript received November 26, 1979; revised December 15, 1979. This work was supported under DOE Contract ET-78-R-03-1876. C. M. Wu's work was supported under NSF Grant ENG78-19426.

The authors are with the Department of Electrical Engineering, Columbia University, New York, NY 10027.